Interactions between pentagonal truncated pyramids with homeotropic anchoring in a nematic liquid crystal

Seyed Reza Seyednejad, Mohammad Reza Mozaffari, Takeaki Araki, and Ehsan Nedaaee Oskoee

Interactions between pentagonal truncated pyramids with homeotropic anchoring in a nematic liquid crystal

Seyed Reza Seyednejad,[1] Mohammad Reza Mozaffari,[2, *]

Takeaki Araki,[3] and Ehsan Nedaaee Oskoee[4]

[1]*Department of Physics, Institute for Advanced Studies*

in Basic Sciences(IASBS), Zanjan 45137-66731, Iran

[2]*Department of Physics, University of Qom, Qom 3716146611, Iran*

[3]*Department of Physics, Kyoto University, Sakyo-ku, Kyoto 606-8502, Japan*

[4]*Research Center for Basic Sciences & Modern Technologies (RBST),*

Institute for Advanced Studies in Basic Sciences(IASBS), Zanjan 45137-66731, Iran

(Dated: August 17, 2018)

Abstract

In this study, we numerically investigate the interactions between pentagonal truncated pyramids in a nematic liquid crystal host. The colloidal arrangements are investigated by minimizing the Landau-de Gennes free energy in presence of homeotropic anchoring surface energy upon the particles. We further explain the interactions using symmetry breaking in the director field and particle-particle relative arrangements. In case of long-range separations, interactions exhibit some deviations from those observed in case of dipolar symmetry. We also exhibit that, in some cases, decreasing the bending elastic distortions between two adjacent lateral faces will cause a non-horizontal side-to-side configuration. In many-body interactions, we evaluate the ability of the bent and branch configurations to form complex self-tiling assemblies pentagonal truncated pyramid blocks.

PACS numbers:

---
*Electronic address: `m.mozaffari@qom.ac.ir`

1

I. INTRODUCTION

The formation of nano- and micro-scale colloidal structures in uniform nematic liquid crystals (NLCs) is generally controlled by anchoring the liquid crystal mesogens on surfaces [1–4] and the shape of the colloids [5–11]. Anchoring causes the director, $\hat{\mathbf{n}}$, around an isolated colloid to be elastically distorted from the uniform orientation in the far-field, $\hat{\mathbf{n}}_0$. Depending on the spatial arrangement and anchoring strength of the molecules at the surface of the colloid, director discontinuities may appear in the form of points or lines in the media in which defects are observed [12].

In spherical geometries, the particle-defect exhibits elastic deformations with dipole or quadrupole symmetries in the electrostatic analogy which decays with distance, D, as D^{-3} or D^{-5}, respectively [1–3, 13–15]. In case of close particle-particle separations, the defects topologically have complex and entangled structures due to symmetry breaking [16, 17] and play a crucial role in anisotropic interactions [13, 18–20]. The self-assembled structure of the colloids is ultimately acquired by the competition between short and long-range colloidal interactions in the nematic host [21–23].

In case of ellipsoids, the aggregations of the elongated and flattened spheroid colloids are specified by the aspect ratios of the ellipsoids [6, 24]. The micro- and nano-rod colloids with homeotropic anchoring are observed to spatially form chain or side-by-side configurations with dipolar and quadrupolar symmetries [5, 25]. The competition between the long-range elastic and electrostatic interactions of nano-rod colloids with positive surface charges leads to triclinic nematic pinacoidal lattices [26].

In a non-spherical case, the low symmetry of the particles cause the NLC elastic deformations around the colloids to be individually reliant on the colloidal shape and spatial arrangements that are relative to the bulk director field. The self-assembly of such colloidal building blocks has drawn considerable attention in both soft condensed matter science and technology [7, 8, 27, 28]. The pentagonal colloidal platelets that are immersed in NLC form quasi-crystalline structures that are known as Penrose tiling patterns [27]. The self-assembly of rectangular and hexagonal micro-sheets with planar anchoring in NLC results in the creation of a large 2D tiling texture [28]. The close contact interactions of platelets exhibit that platelets with quadrupolar elastic deformation are bounded more strongly than the platelets with dipolar symmetry [29]. The faceted nano-cubes and triangular nano-prisms

with homeotropic anchoring induce large disclination loops in NLC, which screw six of the cubic particle edges and two of the triangular faces, respectively [30].

Recently, it has been exhibited that polygonal truncated pyramids (PTPs) can create 2D complex crystalline and quasi-crystalline colloidal structures. In such structures, close contact interactions are observed to be geometrically dependent on the tiling fragments and arrangements, besides, the long-range interactions exhibit a dipolar type, independent of the polygon symmetry [31]. Further, the polygonal platelet colloids with planar anchoring induce dipolar or quadrupolar symmetry when polygons have odd or even side numbers, respectively [7]. The strong binding energy between the blocks results in their stability against external perturbations, this allows the PTP lattices to be considered as candidates for usage in colloidal photonic and electro-optic applications [31]. The rearrangement of the disclination lines at the edges of the polygonal prisms alters the symmetry of director orientation around the colloids and the nature of elastic interactions in the colloidal structures [32]. The self-tiling of the pentagonal truncated pyramids with homeotropic anchoring can also form quasi-crystalline Penrose patterns in contrast to that formed in case of pentagonal platelets with planar anchoring. Thus the PTP colloids that exhibit a low symmetry can display novel kinds of particle-particle interactions with distinct features in NLC. Further, their different spatial arrangements increase their versatility, which allows their usage in different applications.

In this study, we numerically investigate the interactions between pentagonal truncated pyramids (pentagonal-TPs) in a NLC host. We also investigate the colloidal arrangements with homeotropic anchoring by minimizing the Landau-de Gennes free energy. Further, the disclination line defects that are observed around the colloids with different arrangements are also investigated.

II. GEOMETRY

We investigate the colloidal-pair interactions of identical pentagonal truncated pyramids in a uniform NLC, $\hat{\mathbf{n}}_0 = (0, 0, 1)$. The immersed particles also exhibit homeotropic anchoring. In Fig. 1, the radius, $R(= 0.5\mu\mathrm{m})$, is the system length scale that joins the center to one of the vertices in the small pentagonal base. The height, $H(= R/5)$, specifies the distance between the pentagonal bases. In this case, the thickness of the particle would be $H + 2r$
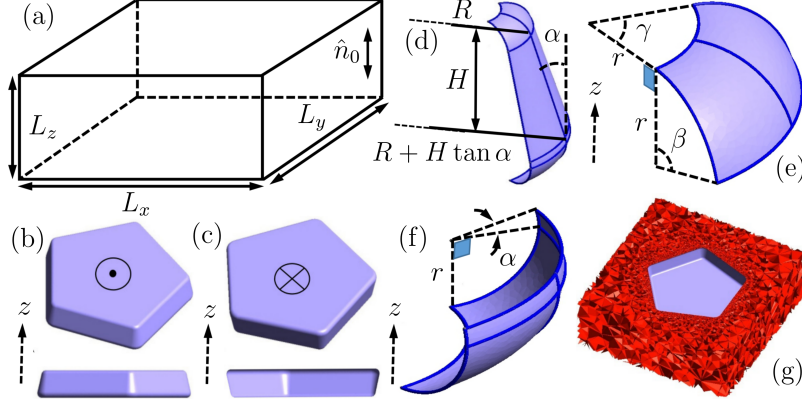
3

FIG. 1: (a) A schematic of the calculation cell. The director has been set parallel to the z-axis at the boundaries. (b) and (c) are respectively parallel and anti-parallel pentagonal truncated pyramids with opposite apex-base direction with respect to the z-axis. (d) A sharp part of the lateral face. α is the angle between lateral edge and height, H. The edges are rounded with roundness radius, r, to keep the director away from unrealistic behaviors. (e) and (f) are the top and bottom parts of (d), respectively, where $\beta = 90° - \alpha$ and $\gamma = 72°$. (g) An adaptive tetrahedral mesh is manually used to perform the finite element method calculations.

where $r(= 0.05R)$ refers to the roundness of the edges. The large base radius can be given as $R + H \tan \alpha$, where α is the tilted angle of the lateral faces. PTPs have been experimentally investigated over a vast range of edge sizes and therefore α angles [31]. Here we use pentagonal-TPs with $\alpha = 15°$ close to what has been experimentally studied. The cell dimensions are $L_x = L_y = 25R$ and $L_z = 15R$.

III. MODEL

We employ a traceless and symmetric tensor order parameter, $Q_{ij}(\vec{r}) = S(\vec{r})(3\hat{n}_i(\vec{r})\hat{n}_j(\vec{r}) - \delta_{ij})/2 + P(\vec{r})(\hat{l}_i\hat{l}_j - \hat{m}_i\hat{m}_j)/2$, to characterize the nematic fluid. The scalar order parameter, S, and the director orientation, $\hat{\mathbf{n}}$, are locally determined by the largest eigenvalue of the tensor order parameter, $\lambda_{max} = S$, and its corresponding eigenvector, respectively. Though the nematic order is observed to be uniaxial, it may be locally biaxial near the surfaces when strong deformations are observed. Generally, the tensor order parameter exhibits three different eigenvalues, $\lambda_1 = -(S + P)/2$, $\lambda_2 = -(S - P)/2$ and $\lambda_3 = \lambda_{max} = S$ with the corresponding eigenvectors of $\hat{l}$, $\hat{m}$ and $\hat{n}(= \hat{l} \times \hat{m})$, respectively ($\lambda_3 > \lambda_2 > \lambda_1$). Thus,

the biaxiality can be given as $P = \lambda_2 - \lambda_1$. Due to the presence of particles with specific anchorings in the uniform nematic host, the director undergoes elastic distortions around the particles. In a uniform nematic phase without an intrinsically biaxial order, biaxiality is observed in the vicinity of defects [33]. The Landau-de Gennes model can explain such distortions in terms of the tensor order parameter and its spatial derivatives as

$$\mathcal{F}_{LdG} = \int_\Omega \mathrm{d}\mathcal{V} \left(\frac{a_0(T - T^*)}{2} Q_{ij}Q_{ji} - \frac{B}{3}Q_{ij}Q_{jk}Q_{ki} \right.$$
$$\left. + \frac{C}{4}(Q_{ij}Q_{ji})^2 + \frac{L_1}{2}\partial_k Q_{ij}\partial_k Q_{ij} \right), \tag{1}$$

where the indices refer to the Cartesian coordinates, the Einstein summation convention is assumed, and Ω refers to the volume of NLC [34]. The initial three terms mainly describe the bulk isotropic-nematic (IN) transition in the thermotropic liquid crystals. It generally determines the equilibrium scalar order parameter, S_{eq}, in terms of temperature, T. The material-dependent coefficients, such as a_0, B, and C, are positive and temperature independent. T^* is the isotropic supercooling temperature. The final term is the contribution of the elastic distortions in the NLC. The constant L_1 is related to the Frank elastic constants using one-constant approximation as $K_{\text{splay}} = K_{\text{twist}} = K_{\text{bend}} = 9L_1 S_{eq}^2/2$ [35]. The normal anchoring effect on the surface of the particles can be given by Nobili's tensorial surface potential as

$$\mathcal{F}_{Surface} = \frac{W}{2} \int_{\partial\Omega} \mathrm{d}\mathcal{S}(Q_{ij} - Q_{ij}^s)(Q_{ji} - Q_{ji}^s), \tag{2}$$

where W is a positive constant that controls the anchoring stiffness, $\partial\Omega$ denotes the area of all the immersed particles in nematic media and the tensor order parameter, $Q_{ij}^s = S_{eq}(3\hat{\nu}_i\hat{\nu}_j - \delta_{ij})/2$, is specified by the preferred direction at the surface, $\hat{\nu}$ [36, 37]. Here, we impose homeotropic anchoring for the case in which $\hat{\nu}$ is a normal unit vector normal to the surface of the pentagonal-TPs. We have chosen the Landau parameters of 5CB as $a_0 = 0.087 \times 10^6 \mathrm{J/m^3 K}$, $T^* = 307.15K$, $T = 305.17K$, $B = -2.12 \times 10^6 \mathrm{J/m^3}$, $C = 1.73 \times 10^6 \mathrm{J/m^3}$, $L_1 = 4 \times 10^{-11} \mathrm{J/m}$, and have imposed strong normal anchoring by choosing $W = 10^{-2} \mathrm{J/m^2}$ [16, 33, 38].

To simplify the calculations, we use dimensionless free energy and rescale the order pa-

rameter as $S = \eta(B/C)\hat{S}$, where $\eta = 1/4$. As a result, the total free energy becomes

$$
\begin{aligned}
\hat{\mathcal{F}} = \frac{\mathcal{F}}{f_0 R^3} = &\int_\Omega \frac{d\mathcal{V}}{R^3} \left(\frac{\tau}{2} q_{ij}q_{ji} - \frac{1}{3\eta} q_{ij}q_{jk}q_{ki} \right. \\
&\left. + \frac{1}{4}\left(q_{ij}q_{ji}\right)^2 - \hat{f}_{eq}(\tau) \right) \\
&+ \frac{1}{2}\frac{\xi^2}{R^2} \int_\Omega \frac{d\mathcal{V}}{R^3} \partial_k q_{ij} \partial_k q_{ij} \\
&+ \frac{1}{2}\frac{w}{R} \int_{\partial\Omega} \frac{d\mathcal{S}}{R^2}(q_{ij} - q_{ij}^s)(q_{ji} - q_{ji}^s),
\end{aligned}
\tag{3}
$$

where $f_0 = \eta^4 B^4/C^3$, $q_{ij} = \hat{S}(3\hat{n}_i\hat{n}_j - \delta_{ij})/2$ is the rescaled tensor order parameter, $\tau = a_0(T - T^*)C/\eta^2 B^2 \simeq -1.05$ is an effective dimensionless temperature, $\hat{f}_{eq}(\tau) = (3\tau/4)\hat{S}_{eq}^2 - (1/4\eta)\hat{S}_{eq}^3 + (9/16)\hat{S}_{eq}^4$ is the dimensionless bulk free energy density in terms of dimensionless temperature, $\hat{S}_{eq} = (1 + \sqrt{1 - 24\tau\eta^2})/6\eta$ is the equilibrium rescaled order parameter, $\xi = \sqrt{L_1 C/\eta^2 B^2} \simeq 0.03R$ is a nematic coherence length and $w = WC/\eta^2 B^2 \simeq 0.122R$ is the anchoring length [39].

IV. NUMERICAL METHOD

A finite element method (FEM) [40] was employed to minimize the total dimensionless free energy. The automatic mesh generator Gmsh [41] was used to decompose the calculation domain into tetrahedral elements. The tensor order parameter elements were further linearly interpolated within each mesh element. The validity of linear interpolation depends on the order parameter deviations within each element that are controlled by the mesh size. As depicted in Fig. 1(e), the tetrahedral elements have been refined around the particle. Recent studies that use the Delaunay triangulation/tetrahedralization algorithm set the element size, L_e, on the particles to $L_e = 0.0025R$ and on the cell boundaries to $L_e = R$ [42]. The conjugate gradient (CG) method [43] is used to minimize the free energy and the iteration steps were terminated when the free energy difference of the two sequential steps dropped below 10^{-10}. For each the spatial orientation of particles, the initial director profile was numerically adopted from the optimized director arrangement of the closest particle-particle separation [40].
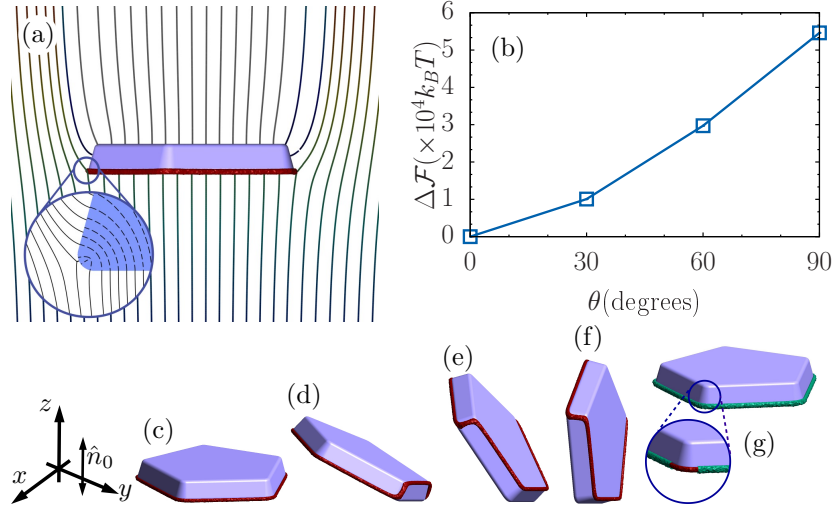
FIG. 2: (a) The director orientation at far distances and around a pentagonal-TP. A disclination line defect of strength $-1/2$ surrounds the object at the large base. The dashed lines in the selected section exhibit the director behavior inside a liquid crystal colloid with a pentagonal-TP shape for boundaries that display homeotropic anchoring. The director lies in the plane and forms a point topological defect of strength $+1/2$ in a disclination line loop. (b) The effective energy of an isolated particle at different spatial arrangements with respect to the $x - y$-plane, (c) $\theta = 0°$, (d) $\theta = 30°$, (e) $\theta = 60°$ and (f) $\theta = 90°$. The free energy difference is given by $\Delta\mathcal{F} = \mathcal{F}(\theta) - \mathcal{F}_{ref}$ where $\mathcal{F}_{ref} = \mathcal{F}(\theta = 0) = 1.950 \times 10^3 k_B T$. For oblique orientations, a part of the closed line defect jumps from the large base to the small base. In all the arrangements, the defect line is observed to pass through sharp edges. The scalar order parameter has been specified for lower than $0.5\hat{S}_{eq}$. (g) The green tube exhibits the biaxiality of the isosurface with $\hat{P} = 0.1$. The tube contains the defect loop.

V. RESULTS

As depicted in Fig. 2(a), the director field deviations, which are due to the normal anchoring on the surface of the particles that are immersed in a uniform nematic media, lead to a closed disclination line defect with a pentagonal shape that surrounds the lateral faces at a large base [31]. In each cross-section of the disclination loop in which the NLC effectively displays a quasi-two-dimensional behavior, the defect structure is formally described by the winding number, $k = \psi/2\pi = -1/2$, where ψ is the amount of rotation of the director around

the defect core in radians [34]. The closed disclination loops of strengths $-1/2$ and $+1/2$ are topologically equivalent to the hyperbolic $m = -1$ and radial $m = +1$ hedgehog charges, respectively [35]. The sum of hedgehog charges, which are due to point defects and disclination loops, is specified by surface Euler characteristic, χ_{Euler}, as $\sum_i m_i = \pm \chi_{\text{Euler}}/2$ [12]. The pentagonal-TP defect charges are similar to those of the spheres in uniformly aligned liquid crystal media with the same Euler characteristic, $\chi_{\text{Euler}} = 2$, and normal boundary conditions [31]. Because of the colloidal geometry, the closed defect does not exhibit a mirror symmetry with respect to the mid-plane of an individual pentagonal-TP. The cost of the elastic distortions ensures that the base of an isolated pentagonal truncated pyramid is always perpendicular to the orientation of the uniform bulk director when homeotropic surface anchoring is imposed on the particle. As shown in Figs. 2(d)- 2(f), the defect line is not bound to the large base in oblique orientation cases. Fig. 2(g) depicts that the biaxial order, $\hat{P}(= (C/\eta B)P)$, is induced only around the edges of the base plate in which the director field is strongly deformed.

In many-body systems, the two-by-two colloidal interactions play an important role in the collective behavior of the particles. Figs. 3 and 4 depict the effective potential energies of two particles versus colloidal center-center distance for cases in which the two pentagonal-TPs approach each other from their flat and tilted faces.

As shown in Fig. 3(g), the pentagonal-TPs attract each other in the parallel ($\odot / \odot$) configurations and repel each other in the anti-parallel ($\odot / \otimes$ or $\otimes / \odot$) configurations when particles approach each other along the same pyramid axis. In each configuration, the long-range interactions exhibit no dependency on the relative colloidal orientations, $\Delta\chi$, and show slight deviations from the dipolar elastic interaction, $(D/R)^{-3}$, where D is the center-center distance. In attractive regimes, the colloids can be influenced by the torques that are applied at the short distances, the non-zero orientations ($\Delta\chi \neq 0$) can lead to Fig. 3(a) by a set of rotational and translational movements. The colloids undergo strong repulsive forces when the small bases are set against each other. Furture, the repulsive interactions are almost independent on the relative colloidal orientations at any separation distance.

In the side-to-side cases that are shown in Figs. 4(a-f), the interactions of two particles have been investigated as a function of distance between parallel pyramid axes. The bottom bases lie in the same plane when they are perpendicular to the far unperturbed director field. In case of large separations, the pentagonal-TPs attract each other in the
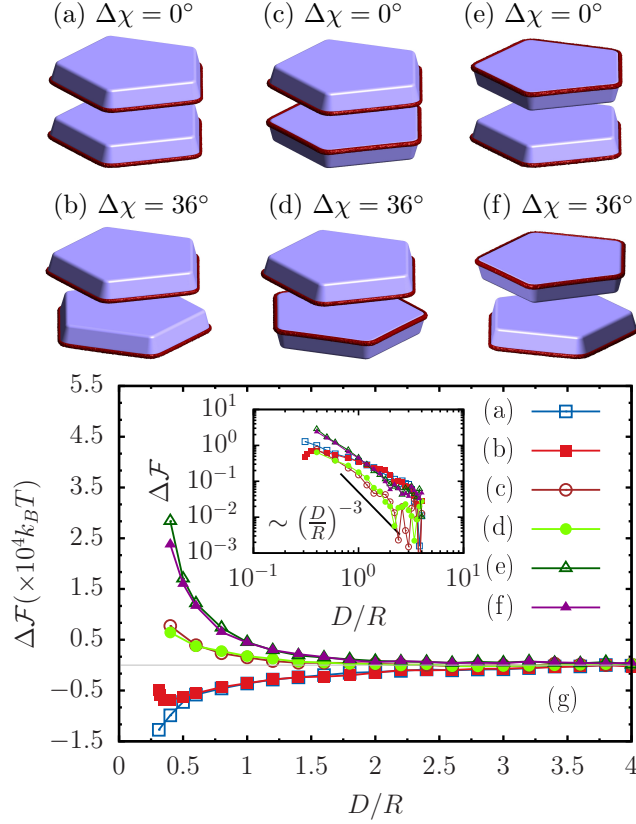
FIG. 3: Interactions of two identical pentagonal-TPs at $\theta = 0°$ with homeotropic anchoring and same pyramid axis in a uniform nematic media. $\Delta\chi$ is the difference between the orientations of the particles around the pyramid axis. (a) and (b) exhibit parallel ($\odot / \odot$) configurations, whereas (c-f) exhibit anti-parallel ($\odot / \otimes$ or $\otimes / \odot$) configurations. (g) The effective potential energies of two particles versus the colloidal center-center distance, D, for the configurations that are shown above. The inset log-log plot compares the long-range interactions with the dipolar potential. The scalar order parameter has been specified for lower than $0.5S_{eq}$.

anti-parallel ($\odot \otimes$) configurations and repel each other in the parallel ($\odot \odot$) configurations (see Fig. 4(g)). Independent of the colloidal interaction types, the free energy potentials have been evaluated by long-range dipolar potential and indicate a fairly good agreement. In parallel configurations, symmetry breaking, which will be discussed in detail later, takes place at small distances so that the repulsive interactions transform into attractive interactions. The configurations that are shown in Figs. 4(e) and (f) are energetically comparable when parallel configurations can overcome the energy barrier, $\sim 0.45 \times 10^4 k_B T$. In configurations 4(a) and (c), symmetry breaking is observed for separations that are smaller than
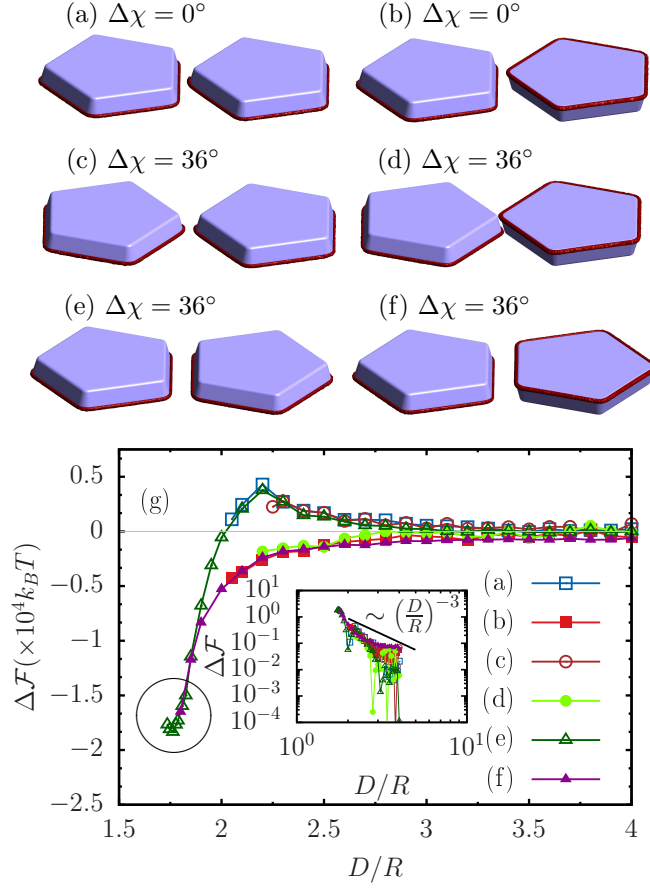
FIG. 4: Interactions of two identical pentagonal-TPs at $\theta = 0°$ with homeotropic anchoring in a uniform nematic media. The particles are arranged side by side when their top bases (or their bottom bases) stand in the same plane. $\Delta\chi$ is the difference between the orientations of the particles around their pyramid axes. (a), (c) and (e) exhibit parallel configurations, ($\odot\odot$). (b), (d) and (f) exhibit anti-parallel configurations, ($\odot\otimes$). (g) The effective potential energies for the above configurations are determined in terms of the distance between the particle axes, D. The inset log-log plot compares the long-range interactions with the dipolar potential. The green triangular points in the circle refer to the non-horizontal states of (e) with $\phi_1 = \phi_2$ which are explained in Fig. 6. The scalar order parameter has been specified for lower than $0.5S_{eq}$.

those depicted in 4(e).

Fig. 5 displays the defect rearrangements in parallel ($\odot\odot$) configurations in case of close contact interactions. Generally, these rearrangements usually change the nature of the interactions at short distances. In Figs. 5(a-c), the splay deformations are the main contribution
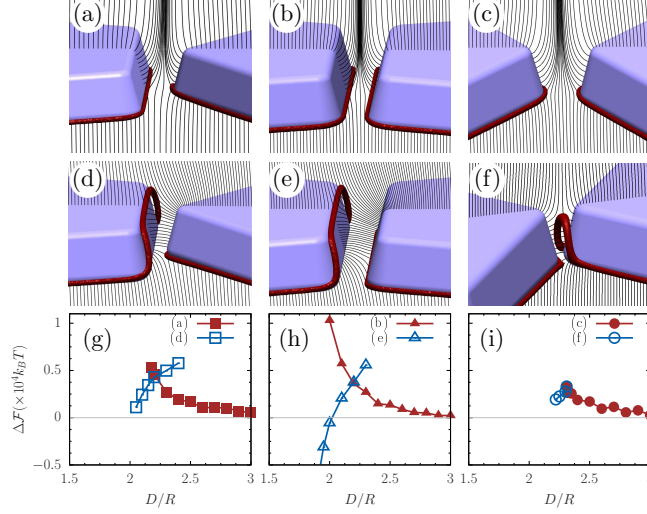
FIG. 5: The defect rearrangements of two identical pentagonal-TPs at small separations with parallel configurations ($\odot \odot$). The particles have been studied at $\theta = 0°$ with homeotropic anchoring in a uniform nematic media. The director orientations and the defect textures at close contact edges and faces are depicted for (a) $\Delta\chi = 0°$ and $D = 2.2R$, (b) $\Delta\chi = 36°$ and $D = 2.0R$, (c) $\Delta\chi = 36°$ and $D = 2.4R$, (d) $\Delta\chi = 0°$ and $D = 2.1R$, (e) $\Delta\chi = 36°$ and $D = 2.0R$, and (f) $\Delta\chi = 36°$ and $D = 2.25R$. The director field is exhibited in 2D planes that include the pentagonal-TP centers and the far-field director alignment. (g)-(i) are the effective potential energies of the parallel configurations ($\odot \odot$) that are mentioned earlier in Fig. 4(g). The energies quantitatively explain the relation between the particle interactions and the defect rearrangement. (g) is the effective potential energy used for investigating the configurations depicted in (a) and (d), (h) is the effective potential energy used for studying the configurations shown in (b) and (e), and (i) is the effective potential energy used for studying the configurations shown in (c) and (f). The scalar order parameter has been specified for lower than $0.5S_{eq}$.

in the elastic distortions when the PTPs approach each other. Indeed, the director around the particles tends to maintain its inherited symmetry from the large separations. In these situations, the disclination line defects are observed at large bases, and the total free energies are observed to display a repulsive behavior (Figs. 5(g-i)). We further manually break the director symmetry in the numerical optimizations by randomly initializing the director field around the particles [44]. As shown in Figs. 5(d) and (e), the bend deformation is observed to become the dominating effect of splay distortion, and the defect loops are rearranged

11

on the lateral faces between particles. Figs. 5(g) and (h) show that the particles attract each other at small separations. Furthermore, an energy level crossing is observed by the superposition of both repulsive and attractive free energy branches. Experimentally, we can switch between repulsive and attractive states by applying laser tweezers that rearrange the disclinations at the edges [32]. In Fig. 5(i), there are meta-stable states at approximately $D = 2.31R$ for which the total energy differences between the 5(c) and (f) configurations are observed to be relatively small and in the order of $10k_BT$. Thus, the transition between the 5(c) and (f) configurations is not continuous but may occur with the slightest thermal fluctuation.

The symmetry breaking causes the configuration in Fig. 4(e) to be an energetically favorable scenario and may cause it to display the reduction in elastic interaction at the cost of more spatial deformations. In that particular case, we are interested in studying those non-horizontal particle orientations in configuration 4(e) at close contact that can decrease the bending elastic distortions between the adjacent lateral faces and slightly increase the bending energy around the bases of the particles. As shown in Fig. 6(a), the large bases show non-zero angles with respect to the horizontal plane as $0 \leq \phi_1 \leq \alpha$ and $\phi_1 \leq \phi_2 \leq 2\alpha - \phi_1$. The effective energy profile in figure 6(b) clearly not only exhibits that the configuration shown in Fig. 4(f) is not the ground state at close contact separation but also that the energy is low for each oblique orientation of particles ($\phi_1, \phi_2 \neq 0$). According to the energy profile, equilibrium configuration occurs at $\phi_1 = \phi_2 \simeq 12.5°$ that causes an entangled defect texture between particles. As shown in Fig. 6(c), two pentagonal disclination line defects are observed to surround the particles near the large bases with two similar side loops and a rectangular frame between close contact lateral faces.

Fig. 7 shows a potential barrier for a collection of parallel configurations from side-to-side ($\odot\odot$) to base-to-base ($\odot/\odot$). Here, we have manually moved the left particle using some translations and rotations(see Figs. 7(b-g)). Numerically, the initial director profile of each spatial particle-particle configuration is chosen using the equilibrium director arrangement of the final closest separation. The potential barrier height ensures that the configurations that are depicted in Figs. 7(a) and (h) exhibit energetically steady states in the short-range elastic interactions and that the transition energy is much larger as compared to the system thermal fluctuations. Therefore, in case of the spatial distribution of each parallel configuration, the final particle-particle arrangement leads to one of the previously mentioned steady states.
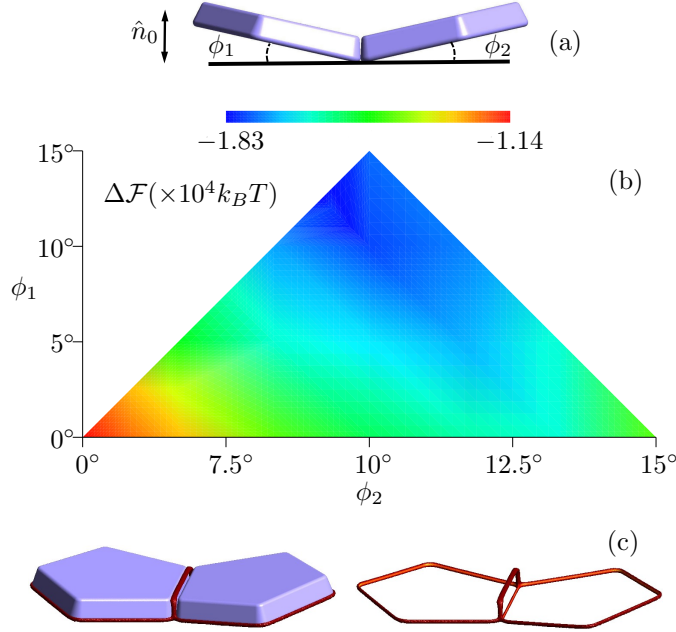
FIG. 6: (a) A non-horizontal schematic of the pentagonal-TPs with the parallel configuration investigated by varing ϕ_1 and ϕ_2. The value of the angles are chosen so that the relation $\phi_1 + \phi_2 \leq 2\alpha$ is satisfied when $\alpha(= 15°)$ is the tilted angle of the lateral faces. For a case in which $\phi_1 + \phi_2 = 2\alpha$, the side faces of the particles are completely in contact with each other. Here, we focus just on the $0 \leq \phi_1 \leq \alpha$ and $\phi_1 \leq \phi_2 \leq 2\alpha - \phi_1$ region and give the $0 \leq \phi_2 \leq \alpha$ and $\phi_2 \leq \phi_1 \leq 2\alpha - \phi_2$ region the same physical treatment. Both the triangle regions exhibit mirror symmetry with respect to the $\phi_1 = \phi_2$ line. The particle-particle separation is $D = 1.8R$ in the case for which $\phi_1 = \phi_2 = 0°$. (b) The effective potential energy profile in terms of the oblique orientation of particles, ϕ_1 and ϕ_2. (c) The entangled disclination line defect in the case for which $\phi_1 = \phi_2 = 12.5°$. The scalar order parameter has been specified for lower than $0.5S_{eq}$.

At the early stages of this path the jumped part of the line defect in Fig. 7(a) leaves the small base and slowly goes back to the large base that causes an increase in free energy. The short-range elastic interactions also induce torques on the pentagonal-TPs at $\Delta\chi = 0°$ and cause their defects to become similar.

In an attempt to understand the complex 2D crystalline and quasi-crystalline self-assemblies by the pentagonal truncated pyramid blocks, we investigated the bent and branch self-tiling patterns when a pentagonal-TP closes to an already assembled structure in a side-
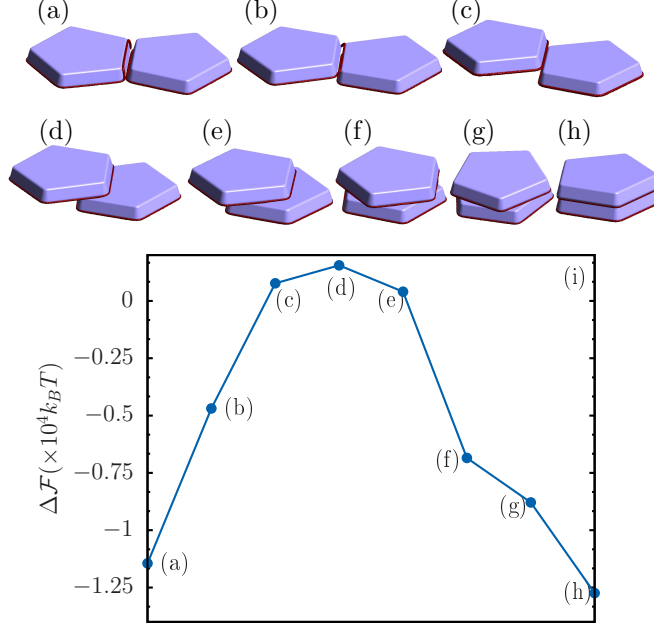
13

FIG. 7: Interaction of two identical pentagonal-TPs at $\theta = 0°$ with homeotropic anchoring for a collection of configurations from side-to-side $\odot\odot$ to base-to-base $\odot/\odot$. Each configuration is specified by a difference in the orientation of the particles around their pyramid axes, $\Delta\chi$, the distance between their pyramid axes, $D^{\perp}$ and the distance between their large bases, $D^{\parallel}$. (a) $\Delta\chi = 36°$, $D^{\perp} = 1.85R$ and $D^{\parallel} = 0$, (b) $\Delta\chi = 36°$, $D^{\perp} = 1.858R$ and $D^{\parallel} = 0.2R$, (c) $\Delta\chi = 36°$, $D^{\perp} = 1.806R$ and $D^{\parallel} = 0.4R$, (d) $\Delta\chi = 36°$, $D^{\perp} = 1.211R$ and $D^{\parallel} = 0.4R$, (e) $\Delta\chi = 36°$, $D^{\perp} = 0.606R$ and $D^{\parallel} = 0.4R$, (f) $\Delta\chi = 36°$, $D^{\perp} = 0$ and $D^{\parallel} = 0.4R$, (g) $\Delta\chi = 18°$, $D^{\perp} = 0$ and $D^{\parallel} = 0.4R$ and (h) $\Delta\chi = 0°$, $D^{\perp} = 0$ and $D^{\parallel} = 0.31R$. (i) The potential barrier between the two minima configurations, (a) and (h). The scalar order parameter has been specified for lower than $0.5S_{eq}$.

to-side fashion. Figs. 8(a) and (b) represent the formations of the bent and branch patterns, respectively. As shown in Fig. 8(c), both the patterns exhibit nearly similar behavior at large and close contact separations. However, the branch patterns provide more favorable conditions for self-tiling at intermediate distances with $\sim 1.67 \times 10^3 k_B T$ energy differences. Such side-to-side long and short elastic interactions of the pentagonal-TP blocks can experimentally form beautiful and known colloidal structures such as ring, diamond, and Penrose tiling [31].
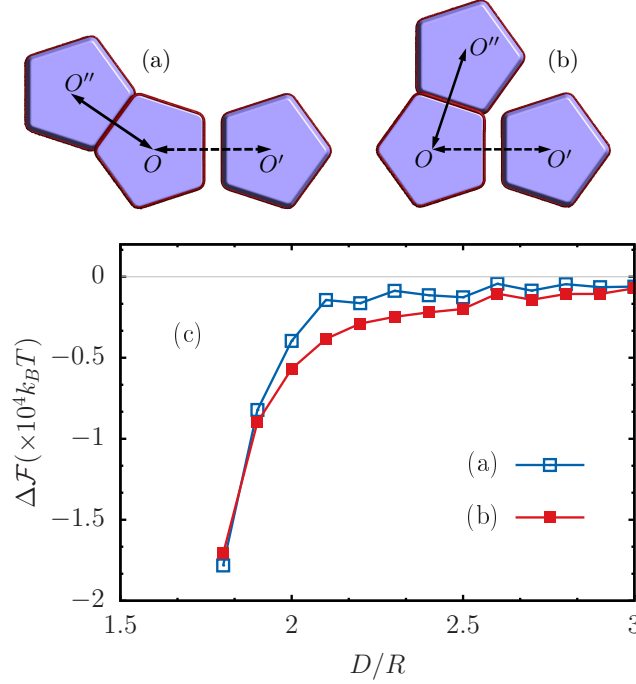
14

FIG. 8: Interaction of a pentagonal-TP with two already-conjoined pentagonal-TPs with an equilibrium distance of $OO'' = 1.8R$, for the bent and branch orientations, (a) $\widehat{O''OO'} = 144°$ and (b) $\widehat{O''OO'} = 72°$. The identical pentagonal-TPs are distributed at $\theta = 0°$ with homeotropic anchoring. (c) The effective potential energy in terms of $OO''(= D)$ separations. The scalar order parameter has been specified for lower than $0.5S_{eq}$.

VI. SUMMARY

We have demonstrated that an isolated pentagonal truncated pyramid with homeotropic anchoring is always perpendicular to the uniform director orientation and that a closed pentagonal line defect having a strength of, $-1/2$, surrounds the lateral face near the large base. The pentagonal-TPs attract each other in the parallel configurations ($\odot$ / $\odot$) and repel each other in the anti-parallel ($\odot$ / $\otimes$ or $\otimes$ / $\odot$) configurations in the base-to-base arrangements. In the side-to-side arrangements, the pentagonal-TPs attract each other in the anti-parallel configurations ($\odot\otimes$) and repel each other in the parallel ($\odot\odot$) configurations. In parallel configurations with small separations, the repulsive interactions are observed to transform into attractive interactions due to symmetry breaking. In this state, the non-horizontal particle orientations at close contact distances decrease the bending elas-

tic distortions between the adjacent lateral faces. We have depicted that the side-to-side ($\odot\,\odot$) and base-to-base ($\odot\,/\,\odot$) configurations are energetically steady and that they do not easily transform into each other. Finally we have compared the ability of bent and branch patterns to form complex self-tiling assemblies using pentagonal truncated pyramid blocks.

[1] P. Poulin, H. Stark, T. C. Lubensky, and D. A. Weitz, Science **275**, 1770 (1997).

[2] M. Yada, J. Yamamoto, and H. Yokoyama, Phys. Rev. Lett. **92**, 185501 (2004).

[3] I. I. Smalyukh, O. D. Lavrentovich, A. N. Kuzmin, A. V. Kachynski, and P. N. Prasad, Phys. Rev. Lett. **95**, 157801 (2005).

[4] I. Musevic, M. Skarabot, U. Tkalec, M. Ravnik, and S. Zumer, Science **313**, 954 (2006).

[5] U. Tkalec, M. Skarabot, and I. Musevic, Soft Matter **4**, 2402 (2008).

[6] F. Mondiot, C. S. Prathap, O. Mondain-Monval, and J.-C. Loudet, Phys. Rev. Lett. **103**, 238303 (2009).

[7] C. P. Lapointe, T. G. Mason, and I. I. Smalyukh, Science **326**, 1083 (2009).

[8] S. Park, Q. Liu, and I. I. Smalyukh, Phys. Rev. Lett. **117**, 277801 (2016).

[9] S. M. Hashemi, U. Jagodic, M. R. Mozaffari, M. R. Ejtehadi, I. Musevic, and M. Ravnik, Nature Communications **8**, 14026 (2017).

[10] Y. Yuan, A. Martinez, B. Senyuk, M. Tasinkevych, and I. I. Smalyukh, Nature Materials **17**, 71 (2017).

[11] I. Musevic, *Liquid Crystal Colloids* (Springer, 2017).

[12] B. Senyuk, Q. Liu, S. He, R. D. Kamien, R. B. Kusner, T. C. Lubensky, and I. I. Smalyukh, Nature **493**, 200 (2012).

[13] R. W. Ruhwandl and E. M. Terentjev, Phys. Rev. E **55**, 2958 (1997).

[14] P. Poulin and D. A. Weitz, Phys. Rev. E **57**, 626 (1998).

[15] I. Musevic and M. Skarabot, Soft Matter **4**, 195 (2008).

[16] M. Ravnik, M. Skarabot, S. Zumer, U. Tkalec, P. I., D. Babic, N. Osterman, and I. Musevic, Phys. Rev. Lett. **99**, 247801 (2007).

[17] B. Senyuk, O. Puls, O. M. Tovkach, S. B. Chernyshuk, and I. I. Smalyukh, Nat. Commun. **7**, 10659 (2016).

[18] T. C. Lubensky, D. Pettey, N. Currier, and H. Stark, Phys. Rev. E **57**, 610 (1998).

[19] T. Araki and H. Tanaka, Phys. Rev. Lett. **97**, 127801 (2006).

[20] M. Skarabot, M. Ravnik, S. Zumer, U. Tkalec, I. Poberaj, D. Babic, N. Osterman, and I. Musevic, Phys. Rev. E **77**, 031705 (2008).

[21] V. G. Nazarenko, A. B. Nych, and B. I. Lev, Phys. Rev. Lett. **87**, 075504 (2001).

[22] J.-C. Loudet, P. Barois, and P. Poulin, Nature **407**, 611 (2000).

[23] I. Musevic, M. Skarabot, D. Babic, N. Osterman, I. Poberaj, V. Nazarenko, and A. Nych, Phys. Rev. Lett. **93**, 187801 (2004).

[24] M. Tasinkevych, F. Mondiot, O. Mondain-Monval, and J.-C. Loudet, Soft Matter **10**, 2047 (2014).

[25] F. R. Hung, B. T. Gettelfinger, J. Gary M. Koenig, N. L. Abbott, and J. J. de Pablo, J. Chem. Phys. **127**, 124702 (2007).

[26] H. Mundoor, B. Senyuk, and I. I. Smalyukh, Science **352**, 69 (2016).

[27] J. Dontabhaktuni, M. Ravnik, and S. Zumer, Proceedings of the National Academy of Sciences **111**, 2464 (2014).

[28] M. V. Rasna, K. P. Zuhail, U. V. Ramudu, R. Chandrasekar, J. Dontabhaktuni, and S. Dhara, Soft Matter **11**, 7674 (2015).

[29] J. Dontabhaktuni, M. Ravnik, and S. Zumer, Soft Matter **8**, 1657 (2012).

[30] F. R. Hung and S. Bale, Molecular Simulation **35**, 822 (2009).

[31] B. Senyuk, Q. Liu, E. Bililign, P. D. Nystrom, and I. I. Smalyukh, Phys. Rev. E **91**, 040501 (2015).

[32] B. Senyuk, Q. Liu, P. D. Nystrom, and I. I. Smalyukh, Soft Matter **13**, 7398 (2017).

[33] S. Kralj, S. Zumer, and D. W. Allender, Phys. Rev. A **43**, 2943 (1991).

[34] P. G. de Gennes and J. Prost, *The physics of liquid crystal* (Oxfor university press, 1995).

[35] M. Kleman and O. D. Lavrentovich, *Soft Matter Physics: An Introduction* (Springer, 2003).

[36] A. Rapini and M. Popoular, J. Phys. (France) **30**, 54 (1969).

[37] M. Nobili and G. Durand, Phys. Rev. A **46**, R6174 (1992).

[38] H. Stark, Physics Reports **351**, 387 (2001).

[39] D. C. Wright and N. D. Mermin, Rev. Mod. Phys. **61**, 385 (1989).

[40] M. R. Mozaffari, M. Babadi, J. Fukuda, and M. R. Ejtehadi, Soft Matter **7**, 1107 (2011).

[41] C. Geuzaine and J.-F. Remacle, International Journal for Numerical Methods in Engineering **79**, 1309 (2009).

[42] S. R. Seyednejad, M. R. Mozaffari, and M. R. Ejtehadi, Phys. Rev. E **88**, 012508 (2013).

[43] W. H. Press, S. A. Teukolsky, W. T. Vetterling, and B. P. Flannery, *Numerical Recipes* (Cambridge University Press, 1992), 2nd ed.

[44] We have also added small random numbers from uniform random distribution in the range

$[-0.01, 0.01]$ to each component of q_{ij} at each mesh point while the traceless condition exists. Further, it has been confirmed that the final solutions are independent of director randomization.